

THE FORMATION OF LARGE-AMPLITUDE FINGERS IN ATMOSPHERIC VORTICES

JASON M. COSGROVE^{✉1} and LAWRENCE K. FORBES¹

(Received 14 April, 2014; accepted 10 July, 2015; first published online 28 March 2016)

Abstract

Large-scale low-pressure systems in the atmosphere are occasionally observed to possess Kelvin–Helmholtz fingers, and an example is shown in this paper. However, these structures are hundreds of kilometres long, so that they are necessarily affected strongly by nonlinearity. They are evidently unstable and are observed to dissipate after a few days.

A model for this phenomenon is presented here, based on the usual f -plane equations of meteorology, assuming an atmosphere governed by the ideal gas law. Large-amplitude perturbations are accounted for, by retaining the equations in their nonlinear forms, and these are then solved numerically using a spectral method. Finger formation is modelled as an initial perturbation to the n th Fourier mode, and the numerical results show that the fingers grow in time, developing structures that depend on the particular mode. Results are presented and discussed, and are also compared with the predictions of the β -plane theory, in which changes of the Coriolis acceleration with latitude are included. An idealized vortex in the northern hemisphere is considered, but the results are at least in qualitative agreement with an observation of such systems in the southern hemisphere.

2010 *Mathematics subject classification*: primary 76B60; secondary 76M22.

Keywords and phrases: atmospheric vortices, spectral methods, f -plane, β -plane.

1. Introduction

Kelvin–Helmholtz flow is a classical problem in fluid mechanics, and it refers to the situation in which two horizontal fluid layers acted on by gravity and separated by a narrow interface move with different mean speeds. As a result, a shearing instability is present at the interface. Small disturbances therefore grow in time, and may eventually develop into *cat's eye* billows, which are large complicated overturning structures. The problem has been the subject of intense study, and is described in the texts by Chandrasekhar [3] and Drazin and Reid [7].

¹School of Physical Sciences, Discipline of Mathematics, University of Tasmania, Private Bag 37, Hobart Tasmania, 7001 Australia; e-mail: Jason.Cosgrove@utas.edu.au, Larry.Forbes@utas.edu.au.
© Australian Mathematical Society 2016, Serial-fee code 1446-1811/2016 \$16.00

Since Kelvin–Helmholtz flow is unstable, it is inevitable that nonlinear effects become important within a finite length of time, because the growing disturbance at the interface eventually becomes of sufficiently large amplitude for the linearized descriptions of it to no longer apply. Moore [16] showed that a curvature singularity is formed at the interface within a finite time in the classical Kelvin–Helmholtz flow in which viscosity is ignored, and Cowley et al. [5] gave an ingenious asymptotic argument to confirm this prediction. Numerical solutions of this problem are found to fail at about the critical time at which the curvature singularity is formed, but Krasny [13] overcame this difficulty using a *vortex blob* method, in which the interface was effectively replaced by a vortex sheet of finite width. His calculations could then proceed beyond the time of singularity formation at the interface, and at later times he obtained the rolled-up surfaces typical of Kelvin–Helmholtz instability. Nevertheless, the problem remains ill-conditioned in some sense, and Baker and Pham [1] demonstrated that different formulations of the vortex blob approach could lead to different solutions at later times.

The curvature singularity at the interface is a consequence of ignoring viscosity. When viscous effects are reintroduced into mathematical models of such unstable flows, the singularity is replaced with a small region of intense vorticity, and this is responsible for the interface rolling up to form overhanging structures. This was demonstrated by Forbes [8] in the related Rayleigh–Taylor instability in which a heavy fluid overlies a lighter one. Chen and Forbes [4] included viscous effects in the classical Kelvin–Helmholtz flow and carried out a careful study of the behaviour of the curvature in the inviscid case and, likewise, showed that, when viscosity is included, the singularity in curvature is replaced with a patch of interfacial vorticity that is ultimately responsible for the formation of overturning *cat's eye* spirals.

Instabilities in cylindrical flow geometries have also been the subject of considerable recent interest. Matsuoka and Nishihara [15] considered an initially cylindrical patch of fluid that is disturbed by a shock, and they showed that several overturning plumes can form in a ring around the originally circular interface. Similar unstable outflows were studied by Forbes [9] in a cylindrical Rayleigh–Taylor flow, in which a light fluid is ejected from a line source into a surrounding heavy fluid.

Instabilities can also occur at the cylindrical interface between two liquids when either or both fluids undergo rotation. Crapper et al. [6] considered the stability of a cylindrical jet undergoing swirling motion with an additional velocity component directed along the axis of the cylinder. This was a linearized analysis in which disturbances to the interface were assumed small. However, Caffisch et al. [2] undertook a nonlinear study of a rotating axisymmetric jet with a line vortex present along its axis. Since the two fluids either side of the interface are moving with different mean angular speeds, a kind of rotational Kelvin–Helmholtz flow instability exists, and Caffisch et al. [2] found that overhanging plumes could develop along the jet. More recently, Forbes and Cosgrove [10] considered planar flow in which a line vortex is present up the z -axis of a Cartesian coordinate system, but an initially cylindrical interface centred on the z -axis separated two fluids of possibly differing densities and angular speeds either side. They carried out a linearized inviscid analysis and

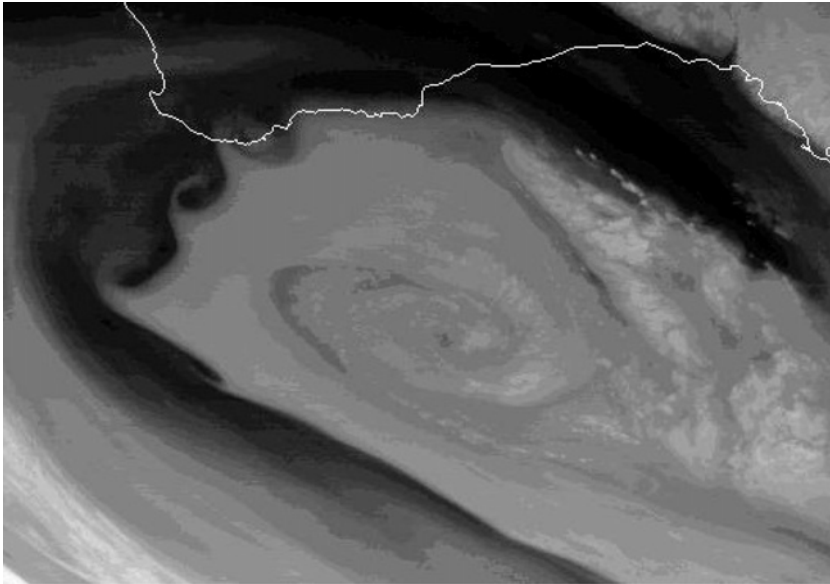


FIGURE 1. Satellite image originally processed by the Bureau of Meteorology from the geostationary meteorological satellite MTSAT-2 operated by the Japan Meteorological Agency, July 2, 2011 0323 GMT.

demonstrated that Kelvin–Helmholtz type instabilities could occur in this cylindrical geometry, in a very similar manner to the classical planar situation discussed by Chandrasekhar [3, p. 485]. Forbes and Cosgrove’s [10] large-amplitude inviscid results were also subject to the formation of a curvature singularity at the interface within finite time, similar to the result of Moore [16] for planar flow. When viscous effects are included in the model, Forbes and Cosgrove [10] could obtain large-amplitude Kelvin–Helmholtz type fingers and billows arranged around the originally circular interface; however, strong mixing occurred and, as time progressed, some of the finger structures evidently even detached from the inner vortex.

It turns out that somewhat similar behaviour is occasionally encountered in meteorological flows. One such example is presented in Figure 1. This flow occurred during July 2011, when a large low-pressure system in the Great Australian Bight moved across the south-west corner of Western Australia; the outline of the coast of the continent is marked as a white line towards the top of this figure. This system rotated clockwise when viewed above from a satellite and, as it rotated, smaller curved fingers formed at the edge and moved around the system, starting at the south-east and moving up and around to the north-west (since this low pressure was situated in the southern hemisphere). The curved fingers are visible towards the upper left corner of this diagram and, although small relative to the overall atmospheric vortex, they, nevertheless, extend some hundreds of kilometres, so representing reasonably large-amplitude disturbances. These fingers were only present for about 4 h and then disappeared.

The present paper therefore seeks to undertake an analysis similar in some respects to that of Forbes and Cosgrove [10], in that moderately large-amplitude instabilities at the edge of a vortex system are of interest. In the present problem, however, the circulation does not arise from a line vortex at the centre of the system, but rather comes about through the Coriolis pseudoacceleration due to the rotation of the Earth. The governing equations are standard, and are outlined briefly in Section 2, for completeness. They consist of the conservation of mass and linear momentum on an appropriate plane tangent to the Earth's surface, but with the Coriolis acceleration term included. Both the f -plane and β -plane approximations will be outlined, in which it is assumed that the Coriolis parameter [17, p. 67] is either constant or else varies linearly with latitude. The numerical method, based on a spectral approach, is described in Section 3, and the results of numerical calculation are presented in Section 4. A discussion in Section 5 concludes the paper.

2. Mathematical formulation

We consider a two-dimensional Cartesian coordinate system. For the f -plane approximation this is a rectangular xy -plane that is tangent to a given point on the Earth's surface. The x -axis is defined to be pointing east and the y -axis pointing north. The origin is located at the tangent point at a given latitude ϕ_0 on the Earth's surface. The left and right sides of the tangent plane are situated at $x = -L$ and $x = L$, respectively, and the top and bottom are located at $y = H$ and $y = -H$, respectively.

The fluid motion is subject to the Coriolis pseudoforce. The Coriolis parameter

$$f = 2\Omega \sin \phi, \quad (2.1)$$

where ϕ is the latitude and the Earth's angular velocity

$$\Omega = 7.292 \times 10^{-5} \text{ s}^{-1}. \quad (2.2)$$

In the northern hemisphere, $f > 0$ and in the southern hemisphere, $f < 0$. The f -plane is the most simple approximation used to study the fluid flow in both the atmosphere and the ocean, and it assumes that the Coriolis parameter f is constant. The value of the Coriolis parameter for the f -plane is determined using the latitude of the tangent point, ϕ_0 in equation (2.1).

The β -plane approximation makes the assumption that the Coriolis parameter f varies linearly with latitude, so that

$$f = f_0 + \beta y,$$

where f_0 is defined by the constant Coriolis parameter for the f -plane (2.1) and β is the rate of change of f and is given by

$$\beta = \frac{2\Omega}{r_e} \cos \phi_0.$$

Here Ω is given by (2.2) and r_e is the radius of the Earth.

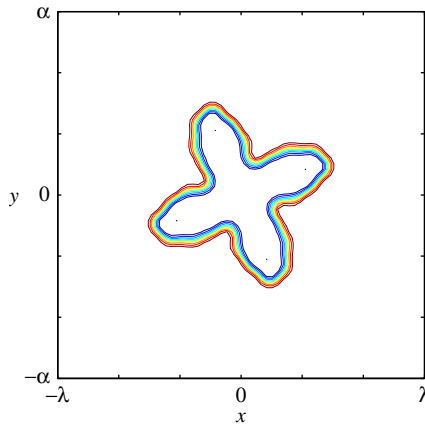


FIGURE 2. Sketch of dimensionless tangent plane. The contours have been taken from an actual solution of pressure with a mode 4 perturbation with perturbation amplitude $a = 0.5$ and Rossby number $Ro_T = 0.15$ at $t = 0.001$.

Dimensionless variables are introduced immediately, and are used throughout this article. All lengths are scaled relative to A , the average initial radius of the pressure system (10^6 m). The density and temperature scales are chosen to be ρ_0 and T_0 , respectively, in which the subscript 0 represents the tangent point on the Earth's surface. Pressure is referenced to the quantity $\rho_0 R T_0$, in which R is the ideal gas constant and takes the value $R = 287.04 \text{ J kg}^{-1} \text{ K}^{-1}$. The time scale is \hat{t} , the approximate number of seconds in one day (10^5 s), and the speed scale is A/\hat{t} . The problem is then found to be dependent on four dimensionless constant parameters,

$$\lambda = \frac{L}{A}, \quad \alpha = \frac{H}{A}, \quad \gamma = \frac{c_p}{c_v}, \quad \nu = \frac{\hat{t}^2 R T_0}{A^2}, \quad (2.3)$$

and two further parameters

$$\omega_0 = f\hat{t}, \quad \omega_1 = \beta A\hat{t} \quad (2.4)$$

that describe aspects of the Coriolis force due to the Earth's rotation. Another parameter of importance later is the time scale Rossby number $Ro_T = 1/\omega_0$, as defined by Vallis [17, p. 85]. It describes the ratio of inertial force to Coriolis force.

The first two constants λ and α in the system (2.3) represent the dimensionless half-width and half-length of the tangent plane, respectively. The constant $\gamma = c_p/c_v$ is the ratio of specific heats, where c_p is the specific heat at a constant pressure and c_v is the specific heat at a constant volume (for an ideal gas, $c_p - c_v = R$, the universal gas constant). The constant parameter ν is a type of inverse Eckert number, which is a ratio of kinetic energy and enthalpy [12, p. 255]. A defining sketch of the dimensionless tangent plane is given in Figure 2.

The constant ω_0 in system (2.4) is the nondimensional Coriolis parameter and is an inverse Rossby number. The last parameter ω_1 is the dimensionless rate of change of f with latitude, and is of interest only in the β -plane description of the flow.

The velocity vector is written as $\mathbf{q} = u\mathbf{e}_x + v\mathbf{e}_y$, where u and v denote the zonal (west–east) and meridional (south–north) velocity components, respectively. The mass conservation equation takes the form

$$\frac{\partial \rho}{\partial t} + u \frac{\partial \rho}{\partial x} + v \frac{\partial \rho}{\partial y} + \rho \left(\frac{\partial u}{\partial x} + \frac{\partial v}{\partial y} \right) = 0. \quad (2.5)$$

The momentum equations for the zonal and meridional velocity components, respectively, are

$$\frac{\partial u}{\partial t} + u \frac{\partial u}{\partial x} + v \frac{\partial u}{\partial y} - \omega_0 v + \frac{v}{\rho} \frac{\partial p}{\partial x} = 0, \quad (2.6)$$

$$\frac{\partial v}{\partial t} + u \frac{\partial v}{\partial x} + v \frac{\partial v}{\partial y} + \omega_0 u + \frac{v}{\rho} \frac{\partial p}{\partial y} = 0. \quad (2.7)$$

It will be assumed that there is no addition of heat per unit mass by external heat sources. This leads to the energy equation

$$\frac{\partial T}{\partial t} + u \frac{\partial T}{\partial x} + v \frac{\partial T}{\partial y} + (\gamma - 1) \frac{p}{\rho} \left(\frac{\partial u}{\partial x} + \frac{\partial v}{\partial y} \right) = 0. \quad (2.8)$$

We will look at perfect fluids that are compressible, so that density ρ is variable. An ideal fluid must obey the equation of state which takes the dimensionless form

$$p = \rho T. \quad (2.9)$$

For consistency, we take the time derivative of the equation of state (2.9), giving an equation for pressure in the form

$$\begin{aligned} \frac{\partial p}{\partial t} = & -T \left[u \frac{\partial \rho}{\partial x} + v \frac{\partial \rho}{\partial y} + \rho \left(\frac{\partial u}{\partial x} + \frac{\partial v}{\partial y} \right) \right] \\ & - \rho \left[u \frac{\partial T}{\partial x} + v \frac{\partial T}{\partial y} + (\gamma - 1) \frac{p}{\rho} \left(\frac{\partial u}{\partial x} + \frac{\partial v}{\partial y} \right) \right]. \end{aligned} \quad (2.10)$$

In summary, the dimensionless governing equations for fluid flow on the f -plane are equations (2.5)–(2.8) and (2.10).

The boundary conditions for the problem are found by looking at time independent, steady state behaviour. To do this, suppose initially that the flow is geostrophic, since much of the atmosphere outside the tropics is close to geostrophic flow [11, p. 30], and that the atmosphere is isothermal. It will also be assumed that the initial steady pressure can be modelled using an exponential function of the form

$$p_s(x, y) = 1 - \mu \exp(-(x^2 + y^2)), \quad (2.11)$$

where μ is a constant that gives the maximum pressure change over the flow region. For the isothermal atmosphere, the constant temperature in dimensionless variables is simply

$$T_s(x, y) = 1. \quad (2.12)$$

The steady pressure (2.11) and constant temperature (2.12) must satisfy the dimensionless equation of state (2.9) and thus the steady density ρ_s takes the same form as the steady pressure

$$\rho_s(x, y) = 1 - \mu \exp(-(x^2 + y^2)) = p_s(x, y) = G(x, y). \quad (2.13)$$

Under the geostrophic flow assumption, the material derivative terms in the governing momentum equations (2.6) and (2.7) can be ignored so that these two equations simplify, approximately, to

$$u_s(x, y) = -\frac{\nu Ro_T}{\rho_s} \frac{\partial p_s}{\partial y} = -\frac{\nu Ro_T}{G(x, y)} \frac{\partial G}{\partial y}, \quad (2.14)$$

$$v_s(x, y) = \frac{\nu Ro_T}{\rho_s} \frac{\partial p_s}{\partial x} = \frac{\nu Ro_T}{G(x, y)} \frac{\partial G}{\partial x}. \quad (2.15)$$

As the flow on the outer edges of the tangent plane has minimal influence on the flow in the centre of the tangent plane, the equations (2.11)–(2.15) must hold on the edges at $x = \pm\lambda$ and $y = \pm\alpha$ of the tangent plane and thus these equations double as boundary conditions to the fully nonlinear flow.

The mass conservation equation (2.5), the thermodynamic equation (2.8) and the equation of state (2.10) are unaltered for the β -plane approximation. The zonal and meridional momentum equations (2.6) and (2.7) differ slightly as the ω_0 term is replaced with $\omega_0 + \omega_1 y$ to give

$$\frac{\partial u}{\partial t} + u \frac{\partial u}{\partial x} + v \frac{\partial u}{\partial y} - v(\omega_0 + \omega_1 y) + \frac{\nu}{\rho} \frac{\partial p}{\partial x} = 0, \quad (2.16)$$

$$\frac{\partial v}{\partial t} + u \frac{\partial v}{\partial x} + v \frac{\partial v}{\partial y} + u(\omega_0 + \omega_1 y) + \frac{\nu}{\rho} \frac{\partial p}{\partial y} = 0. \quad (2.17)$$

The governing equations for fluid flow on the β -plane are thus (2.5), (2.8), (2.10), (2.16) and (2.17). The boundary conditions for the β -plane approximation are the same as for the f -plane approximation.

3. The spectral solution method

In this section, a spectral solution for the five variables that are needed in order to solve the problem at hand will be discussed. The variables for pressure p , density ρ , temperature T zonal velocity u and meridional velocity v are written as the sum of a steady time-independent background flow component and a fully unsteady time

dependent component in the form

$$\begin{aligned}
 p(x, y, t) &= p_s(x, y) + p_u(x, y, t), \\
 \rho(x, y, t) &= \rho_s(x, y) + \rho_u(x, y, t), \\
 T(x, y, t) &= T_s(x, y) + T_u(x, y, t), \\
 u(x, y, t) &= u_s(x, y) + u_u(x, y, t), \\
 v(x, y, t) &= v_s(x, y) + v_u(x, y, t).
 \end{aligned}$$

The steady background components are denoted with the subscript s , and are given by the equations (2.11)–(2.15) which also double as the boundary conditions for both the f -plane and β -plane approximations. Thus the fully nonlinear representation of the variables is

$$u(x, y, t) = -\frac{\nu Ro_T}{G(x, y)} \frac{\partial G}{\partial y} + \sum_{m=1}^{\infty} \sum_{n=1}^{\infty} A_{mn}(t) \sin\left(\frac{m\pi(x + \lambda)}{2\lambda}\right) \sin\left(\frac{n\pi(y + \alpha)}{2\alpha}\right), \quad (3.1)$$

$$v(x, y, t) = \frac{\nu Ro_T}{G(x, y)} \frac{\partial G}{\partial x} + \sum_{m=1}^{\infty} \sum_{n=1}^{\infty} B_{mn}(t) \sin\left(\frac{m\pi(x + \lambda)}{2\lambda}\right) \sin\left(\frac{n\pi(y + \alpha)}{2\alpha}\right), \quad (3.2)$$

$$p(x, y, t) = G(x, y) + \sum_{m=1}^{\infty} \sum_{n=1}^{\infty} P_{mn}(t) \sin\left(\frac{m\pi(x + \lambda)}{2\lambda}\right) \sin\left(\frac{n\pi(y + \alpha)}{2\alpha}\right), \quad (3.3)$$

$$\rho(x, y, t) = G(x, y) + \sum_{m=1}^{\infty} \sum_{n=1}^{\infty} R_{mn}(t) \sin\left(\frac{m\pi(x + \lambda)}{2\lambda}\right) \sin\left(\frac{n\pi(y + \alpha)}{2\alpha}\right), \quad (3.4)$$

$$T(x, y, t) = 1 + \sum_{m=1}^{\infty} \sum_{n=1}^{\infty} T_{mn}(t) \sin\left(\frac{m\pi(x + \lambda)}{2\lambda}\right) \sin\left(\frac{n\pi(y + \alpha)}{2\alpha}\right). \quad (3.5)$$

The coefficient functions $A_{mn}(t)$, $B_{mn}(t)$, $P_{mn}(t)$, $R_{mn}(t)$ and $T_{mn}(t)$ are to be determined. In equations (3.3) and (3.4) the function $G(x, y)$ is given by (2.13) and its partial derivatives with respect to x and y are used in equations (3.2) and (3.1), respectively.

Using the nonlinear representation (3.4), the mass equation (2.5) can be rearranged so that

$$\frac{\partial \rho}{\partial t} = \sum_{m=1}^{\infty} \sum_{n=1}^{\infty} R'_{mn}(t) \sin\left(\frac{m\pi(x + \lambda)}{2\lambda}\right) \sin\left(\frac{n\pi(y + \alpha)}{2\alpha}\right) = -F_1(x, y, t), \quad (3.6)$$

where

$$F_1(x, y, t) = u \frac{\partial \rho}{\partial x} + v \frac{\partial \rho}{\partial y} + \rho \left(\frac{\partial u}{\partial x} + \frac{\partial v}{\partial y} \right). \quad (3.7)$$

The function $F_1(x, y, t)$ is simply the nonlinear terms in the mass equation (2.5). At this point, it is necessary to derive a system of ordinary differential equations for the time dependent Fourier coefficients, $R_{mn}(t)$. This is done in a similar manner to Forbes [8]. The equation (3.6) is spectrally decomposed by multiplying by basis functions and

integrating over the region of the tangent plane $-\lambda < x < \lambda$, $-\alpha < y < \alpha$. This gives the system of differential equations

$$R'_{kl}(t) = \frac{-1}{\lambda\alpha} \int_{-\lambda}^{\lambda} \int_{-\alpha}^{\alpha} F_1 \sin\left(\frac{k\pi(x + \lambda)}{2\lambda}\right) \sin\left(\frac{l\pi(y + \alpha)}{2\alpha}\right) dy dx$$

for $k = 1, 2, \dots, M$, and $l = 1, 2, \dots, N$. (3.8)

This procedure is replicated to derive systems of ordinary differential equations for the remaining Fourier coefficients, $A_{mn}(t)$, $B_{mn}(t)$, $P_{mn}(t)$ and $T_{mn}(t)$. For brevity, they will only be stated here. The momentum equations (2.6) and (2.7) give rise to the system of differential equations

$$A'_{kl}(t) = \frac{\nu}{\lambda\alpha} \int_{-\lambda}^{\lambda} \int_{-\alpha}^{\alpha} \frac{1}{G(x, y)} \frac{\partial G}{\partial x} \sin\left(\frac{k\pi(x + \lambda)}{2\lambda}\right) \sin\left(\frac{l\pi(y + \alpha)}{2\alpha}\right) dy dx$$

$$- \frac{1}{\lambda\alpha} \int_{-\lambda}^{\lambda} \int_{-\alpha}^{\alpha} F_2(x, y, t) \sin\left(\frac{k\pi(x + \lambda)}{2\lambda}\right) \sin\left(\frac{l\pi(y + \alpha)}{2\alpha}\right) dy dx + \omega_0 B_{kl}(t)$$

for $k = 1, 2, \dots, M$, and $l = 1, 2, \dots, N$, (3.9)

$$B'_{kl}(t) = \frac{\nu}{\lambda\alpha} \int_{-\lambda}^{\lambda} \int_{-\alpha}^{\alpha} \frac{1}{G(x, y)} \frac{\partial G}{\partial y} \sin\left(\frac{k\pi(x + \lambda)}{2\lambda}\right) \sin\left(\frac{l\pi(y + \alpha)}{2\alpha}\right) dy dx$$

$$- \frac{1}{\lambda\alpha} \int_{-\lambda}^{\lambda} \int_{-\alpha}^{\alpha} F_3(x, y, t) \sin\left(\frac{k\pi(x + \lambda)}{2\lambda}\right) \sin\left(\frac{l\pi(y + \alpha)}{2\alpha}\right) dy dx - \omega_0 A_{kl}(t)$$

for $k = 1, 2, \dots, M$, and $l = 1, 2, \dots, N$, (3.10)

and the differentiated equation of state (2.10) yields

$$P'_{kl}(t) = \frac{-1}{\lambda\alpha} \int_{-\lambda}^{\lambda} \int_{-\alpha}^{\alpha} F_4(x, y, t) \sin\left(\frac{k\pi(x + \lambda)}{2\lambda}\right) \sin\left(\frac{l\pi(y + \alpha)}{2\alpha}\right) dy dx$$

for $k = 1, 2, \dots, M$, and $l = 1, 2, \dots, N$. (3.11)

Finally, the energy equation (2.8) results in the system

$$T'_{kl}(t) = \frac{-1}{\lambda\alpha} \int_{-\lambda}^{\lambda} \int_{-\alpha}^{\alpha} F_5(x, y, t) \sin\left(\frac{k\pi(x + \lambda)}{2\lambda}\right) \sin\left(\frac{l\pi(y + \alpha)}{2\alpha}\right) dy dx$$

for $k = 1, 2, \dots, M$, and $l = 1, 2, \dots, N$. (3.12)

In these expressions, the nonlinear terms

$$F_2(x, y, t) = uu_x + vu_y + vp_x/\rho$$

$$F_3(x, y, t) = uv_x + vv_y + vp_y/\rho$$

$$F_5(x, y, t) = uT_x + vT_y + (\gamma - 1)p(u_x + v_y)/\rho$$

$$F_4(x, y, t) = TF_1(x, y, t) + \rho F_5(x, y, t)$$

(3.13)

have been defined for convenience, where $F_1(x, y, t)$ is given in equation (3.7). The equations (3.8)–(3.12) constitute a system of $5MN$ ordinary differential equations for the time dependent Fourier coefficients in the representations for the zonal

velocity (3.1), the meridional velocity (3.2), the pressure (3.3), the density (3.4) and the temperature (3.5). This large system of differential equations is then solved using a fourth-order Runge–Kutta method to integrate the coefficients forward in time.

The variables for the zonal velocity u , meridional velocity v , pressure p , density ρ and temperature T for the β -plane approximation have the same form as for the f -plane, and are represented by equations (3.1)–(3.5). However, the Fourier coefficients $A_{mn}(t)$, $B_{mn}(t)$, $P_{mn}(t)$, $R_{mn}(t)$ and $T_{mn}(t)$ will change. For the β -plane, the ordinary differential equations used to determine the Fourier coefficients $P_{mn}(t)$, $R_{mn}(t)$ and $T_{mn}(t)$ are the same as for the f -plane. The equations for the coefficients $A_{mn}(t)$ and $B_{mn}(t)$ are the same as (3.9) and (3.10), except that now the appropriate intermediate functions in (3.13) are replaced by

$$\begin{aligned} F_2(x, y, t) &= uu_x + vu_y - \omega_1 yv + vp_x/\rho \\ F_3(x, y, t) &= uv_x + vv_y + \omega_1 yu + vp_y/\rho, \end{aligned}$$

as required by equations (2.16) and (2.17) in the β -plane. The remaining differential equations (3.8), (3.11) and (3.12) are unaltered.

4. Presentation of results

Throughout this section, results will be presented by means of pressure contour maps, as is common in meteorological charts. Solutions will be given for different latitudes, and hence varying Rossby numbers and different perturbation modes and amplitudes will be of interest. We have also compared pressure maps with density contour diagrams, and the two are closely similar, as is to be expected from the ideal gas law (2.9). A comparison of the results obtained from the f -plane approximation to the β -plane approximation will also be studied, in order to observe qualitative differences between both approximations. The Rossby numbers considered in this paper will be either $Ro_T = 0.1$ or $Ro_T = 0.15$ and are either constant throughout the entire region of the f -plane approximation, or else take this value at $y = 0$ for the β -plane approximation. These two Rossby numbers are chosen so that comparisons between mid latitudes and mid–low latitude regions can be made. The Rossby number $Ro_T = 0.15$ corresponds to a tangent point at the mid–low latitude $\phi \approx 27.2^\circ$, and thus shows flow behaviour for mid–low latitude regions. The nature of mid-latitude fluid flow can be studied by considering Rossby number $Ro_T = 0.1$ which corresponds to a tangent point at the mid latitude $\phi \approx 43.3^\circ$. Since $Ro_T > 0$, we are looking at f -plane and β -plane approximations in the northern hemisphere.

Lipps [14] states that, for the β -plane approximation to be valid,

$$Ro_T = \frac{1}{\omega_0} \ll 1, \quad \omega_1 = \beta A \hat{t} \sim 1. \quad (4.1)$$

Clearly, the first condition in (4.1) is met through the choice of Rossby numbers used in this study. For $Ro_T = 0.1$ and $Ro_T = 0.15$, the respective ω_1 values are 1.667 and 2.036, and these are consistent with the second condition in (4.1).

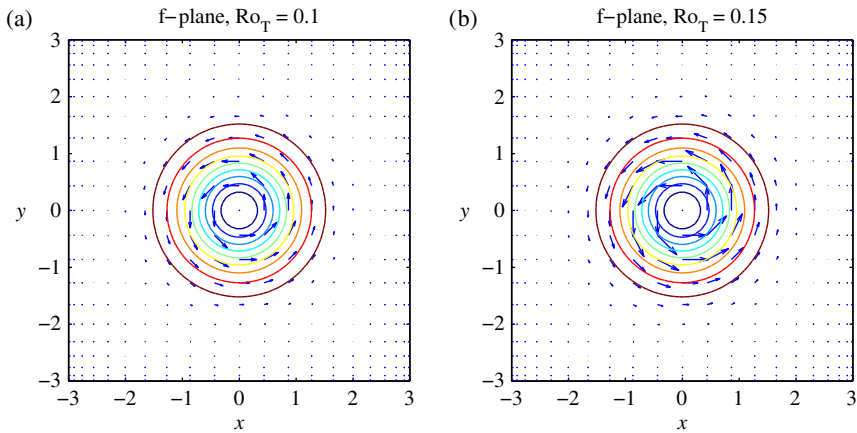


FIGURE 3. Steady pressure contour plots and quiver plots of steady velocity on the f -plane with Rossby numbers (a) $Ro_T = 0.1$ (b) $Ro_T = 0.15$.

The dimensionless half-plane width and length will be $\lambda = 3$ and $\alpha = 3$, respectively. The density scale was taken to be $\rho_0 = 1.213 \text{ kg m}^{-3}$, the temperature scale was $T_0 = 290 \text{ K}$ and, therefore, the pressure scale $\rho_0 RT_0 = 1 \text{ atm} = 1.01 \times 10^5 \text{ Pa}$. The ratio of specific heats is taken to be $\gamma = 1.4$, and the maximum dimensionless pressure drop is $\mu = 0.1$.

Contour plots of the steady pressure p_s in equation (2.11) together with quiver plots of the steady velocity components in equations (2.14) and (2.15) for an f -plane approximation are shown in Figure 3. This figure depicts geostrophic balance, where the Coriolis effect and the pressure gradient force are equal. Figures 3(a) and (b) were produced using Rossby numbers $Ro_T = 0.1$ and $Ro_T = 0.15$, respectively. In the pressure contour plots, the blank outer region has pressure ranging from 0.99 to 1.00, the blank inner region has pressure in the range 0.90–0.91 and the visible contours have values that increase in increments of 0.01 from 0.91 to 0.99. These contour values are used in all subsequent contour plots. The velocity for the f -plane approximation with $Ro_T = 0.15$ is exactly 50% larger than with $Ro_T = 0.1$, and this is illustrated in Figure 3, with the longer arrows in Figure 3(b) compared with 3(a). In the northern hemisphere, low-pressure systems rotate in an anticlockwise direction, which has been confirmed by the quiver plot in these figures. A consequence of geostrophic flow is that the geostrophic velocity vector is parallel to lines where pressure is constant. This is also confirmed in both Figures 3(a) and 3(b) as the quivers are aligned tangentially to the contours of the steady pressure. In the interest of brevity, the β -plane velocity plots are not shown here.

For the f -plane approximation, the quivers are antisymmetric about $y = 0$. This is not the case for the β -plane as the Rossby number varies as a function of latitude. For the β -plane approximation, the closer to the equator the greater the Rossby number. When comparing the f -plane and β -plane approximations that have the same Rossby

TABLE 1. Shows the dimensionless fluid velocity on the β -plane and f -plane for a selected number of latitude coordinates y , with $Ro_T = 0.1$ and $Ro_T = 0.15$ at $y = 0$.

Latitude coordinate y	Dimensionless fluid velocity at $x = 0$			
	f -plane speed $Ro_T = 0.1$	β -plane speed $Ro_T = 0.1$ at $y = 0$	f -plane speed $Ro_T = 0.15$	β -plane speed $Ro_T = 0.15$ at $y = 0$
3.0	0.0070	0.0047	0.0105	0.0055
2.5	0.0929	0.0659	0.1394	0.0795
1.4	3.3746	2.7387	5.0619	3.5505
0.5	6.9020	6.3899	10.3530	9.0264
0	0.0000	0.0000	0.0000	0.0000
-0.5	6.9020	7.5034	10.3530	12.1353
-1.4	3.3746	4.3952	5.0619	8.8124
-2.5	0.0929	0.1579	0.1394	0.5661
-3.0	0.0070	0.0139	0.0105	0.1158

number at $y = 0$, the velocities at the same coordinate vary significantly. This is especially the case for the larger Rossby number $Ro_T = 0.15$. In the southern half of the approximation regions the velocities for identical points are greater for the β -plane than for the f -plane, and vice versa in the northern half. If $Ro_T = 0.15$, on $y = 0$ the velocities on the β -plane are approximately 11 times faster than those on the f -plane, and at the southern latitude $y = -3$ the speeds are about half the values at the same northern latitude $y = 3$. Table 1 shows the dimensionless fluid velocities on the f -plane and β -planes for a selected number of y -coordinates, with $Ro_T = 0.1$ and $Ro_T = 0.15$ at $y = 0$. These results are the major influence on the differences observed between the f -plane and β -plane solutions.

The initial conditions for the nonlinear fluid flow in the f -plane and β -plane approximations were determined by assuming that the fluid flow was initially geostrophic and therefore its velocity was just the steady background velocity. This is achieved by setting $A_{mn}(0) = B_{mn}(0) = 0$ in equations (3.1) and (3.2). Similarly, initially the atmosphere is assumed to be isothermal so that the temperature is again just the steady background temperature $T = 1$, and thus $T_{mn}(0) = 0$ in equation (3.5). It then follows from equation (2.9) that the pressure p and density ρ are equal at $t = 0$. The initial pressure and density are perturbed and are assumed to be

$$p(x, y, 0) = \rho(x, y, 0) = \begin{cases} 1 & \text{if } r > 1 + a \sin n\theta \\ 1 - \mu & \text{if } r < 1 + a \sin n\theta. \end{cases} \quad (4.2)$$

In equation (4.2), the variable μ is the maximum pressure drop, n is the perturbation mode, a is the perturbation amplitude and

$$r = \sqrt{x^2 + y^2}.$$

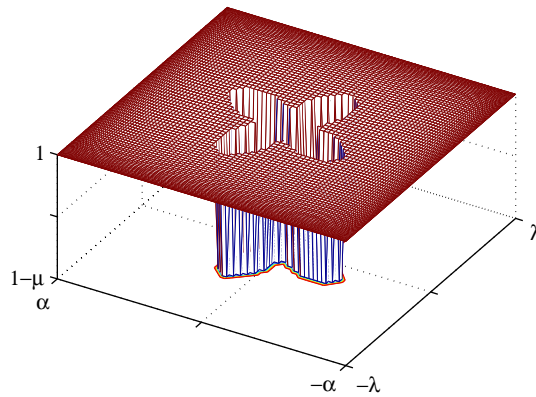


FIGURE 4. Sketch of 3-dimensional initial pressure and density profile for a mode 4 perturbation with perturbation amplitude $a = 0.5$ and Rossby number $Ro_T = 0.15$.

Numerous perturbation modes have been studied in this research together with perturbation amplitudes $a = 0.1$, $a = 0.25$ and $a = 0.5$.

Figure 4 shows a three-dimensional plot of the initial pressure and density for a mode four perturbation with amplitude $a = 0.5$ and pressure drop μ . Spectral decomposition is used to find the initial values of the Fourier coefficients $P_{mn}(0)$ and $R_{mn}(0)$ for the pressure and density functions. Thus

$$P_{mn}(0) = \frac{1}{\lambda\alpha} \int_{-\lambda}^{\lambda} \int_{-\alpha}^{\alpha} [p(x, y, 0) - G(x, y)] \sin\left(\frac{m\pi(x + \lambda)}{2\lambda}\right) \sin\left(\frac{n\pi(y + \alpha)}{2\alpha}\right) dy dx. \quad (4.3)$$

The form of the coefficients $R_{mn}(0)$ is identical, except that $p(x, y, 0)$ is replaced with $\rho(x, y, 0)$ in the integrand of equation (4.3). The quadratures are performed using the Gaussian integration routine provided by von Winckel [18].

In the fully nonlinear solution, there are initially two distinct regions of pressure, one of low pressure ($p = 1 - \mu$) and one of a higher pressure ($p = 1$). These two regions are separated by an interface, which is distinguished by a smooth but rapid change in pressure p , so that contours of this function are closely packed together in that zone. As the pressure difference between both regions is given by the maximum pressure drop μ , it makes sense to distinguish the boundary between both regions as the contour value of the average pressure. Therefore, the effective interface is defined to be the location of the pressure contour $p = 1 - \mu/2$. In our case, where the pressure drop $\mu = 0.1$, the interfacial pressure is the contour value $p = 0.95$.

For all perturbation modes and amplitudes considered in this paper, as time increases it is found that the pressure interface undergoes oscillations until it becomes essentially circular, suggesting that it is approaching a geostrophic balance. The initial perturbation amplitude impacts on both the oscillation amplitudes and the time it takes for the pressure to reach its steady state. The larger the initial amplitude the greater the time to reach stability, and this is illustrated in Figure 5.

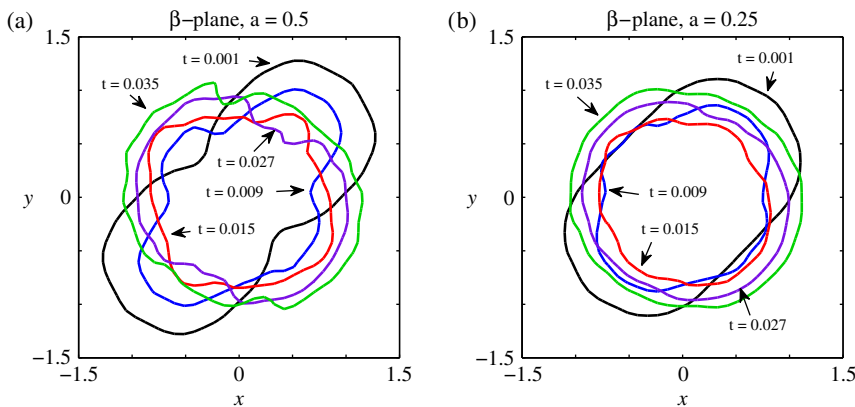


FIGURE 5. Interfacial pressure plot on the β -plane for a mode 2 perturbation with Rossby number $Ro_T = 0.15$ at times $t = 0.001, 0.009, 0.015, 0.027$ and 0.035 with perturbation amplitudes (a) $a = 0.5$ and (b) $a = 0.25$.

Figure 5(a) shows the evolution of the interfacial pressure for a mode two perturbation with perturbation amplitude $a = 0.5$ and Rossby number $Ro_T = 0.15$ on $y = 0$ at $t = 0.001, 0.009, 0.015, 0.027$ and 0.035 on the β -plane. At $t = 0.001$, the interface is elliptical in nature with the major axis oriented in a south-west to north-east direction and the minor axis is oriented in a south-east to north-west direction. As the time increases to $t = 0.035$, the interfacial pressure contour is almost circular, apart from two dips in the north and south regions. In contrast, the smaller perturbation amplitude $a = 0.25$ shown in Figure 5(b) has an essentially circular interfacial pressure contour at $t = 0.015$ and beyond.

Although not shown here, the evolution of the interfacial pressure is very similar for the f -plane approximation; however, there is a much smoother transition to the stable circular shape, particularly in the south-east quadrant for the β -plane approximation.

The predictions of the f -plane and β -plane models are contrasted in Figure 6. As the f -plane approximation uses a constant Coriolis parameter, the pressure contour plots exhibit rotational symmetry of order n about the origin of the plane, where n is the perturbation mode. This rotational symmetry is illustrated in Figure 6(a), which shows the pressure contours of a mode six perturbation with Rossby number $Ro_T = 0.15$ at time $t = 0.018$, from the f -plane equations. This is the time at which there is a clear finger structure on the outer rim of the pressure system. In this paper, we will define the time of finger formation as the greatest time at which the interfacial pressure contour $p = 0.95$ has one closed contour and is shown by the bold contour in Figure 6(a). The contours of the pressure $p(x, y, t)$ were computed using equation (3.3).

In contrast, the β -plane approximation has a Coriolis parameter that varies linearly with latitude and, consequently, the pressure contour plots do not exhibit the rotational symmetry observed in the f -plane pressure plots. This lack of symmetry can be seen in Figure 6(b), which shows the pressure contour plots of the β -plane equivalent

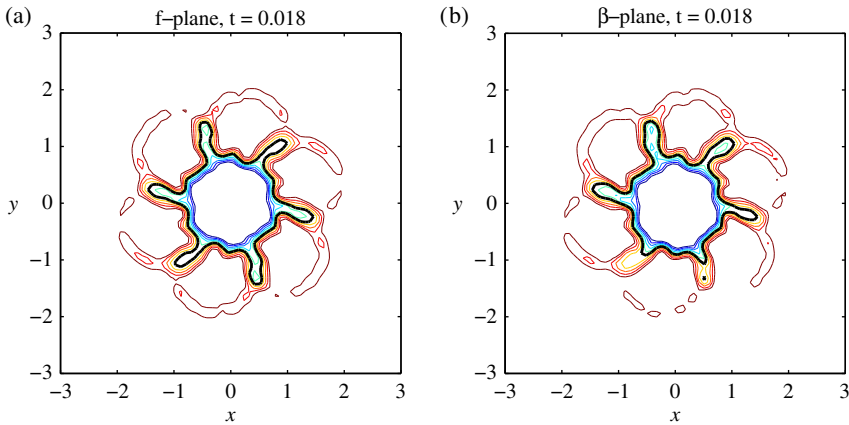


FIGURE 6. Pressure contour plots with interfacial pressure in bold for a mode 6 perturbation and perturbation amplitude $a = 0.5$ at time $t = 0.018$ for (a) f -plane with constant Rossby number $Ro_T = 0.15$ and (b) β -plane with Rossby number $Ro_T = 0.15$ on $y = 0$.

to Figure 6(a). The most noticeable differences occur in the northern region from $1 < y < 3$ and the southern region from $-3 < y < -1$. In the northern region, the Rossby number $Ro_T < 0.15$, and thus the fluid speed is less than the corresponding speed in the same region of the f -plane. This enables the pressure regions to maintain their profile and not disperse easily. The opposite is true for the southern region, where the Rossby number $Ro_T > 0.15$ and therefore the speed of the fluid is greater than for the fluid on the f -plane in the same region. This greater speed enables the pressure to convect more rapidly on the β -plane and enables finger structures to form and deteriorate more quickly. This can be seen in the southern half of Figure 6(b), where the finger structure observed for the f -plane is nonexistent for the β -plane in this region. The isolated $p = 0.95$ contour indicates that the finger has broken off at this time for the β -plane. In fact, for this configuration, finger formation occurs at the earlier time $t = 0.017$. The time itself is marginally less than for the f -plane but the finger length is considerably smaller. This result is consistent for all perturbation modes and amplitudes $a = 0.5$ and $a = 0.25$. In the central region $-1 < y < 1$, where the Rossby number $Ro_T \approx 0.15$, the flow behaviour and pressure structure are almost identical, as expected. The observed differences can be attributed to the β -effect, which indicates how fluid motion is affected by changes of the Coriolis parameter with respect to latitude. When $Ro_T = 0.15$ on $y = 0$, then the β -plane Rossby numbers increase from $Ro_T = 0.0783$ at $y = 3$ up to $Ro_T = 1.7834$ at $y = -3$.

The β -effect is almost indistinguishable in the mid-latitude regions. If $Ro_T = 0.1$ on $y = 0$, then the β -plane approximation is almost identical to the f -plane approximation. Figures 7(a) and (b) are the respective pressure contour plots for an f -plane and β -plane approximation for a mode five perturbation with perturbation amplitude $a = 0.5$ at time $t = 0.022$. The only real differences between the f -plane and β -plane contour diagrams are the subtle changes in the pressure contour $p = 0.99$ in the south-east

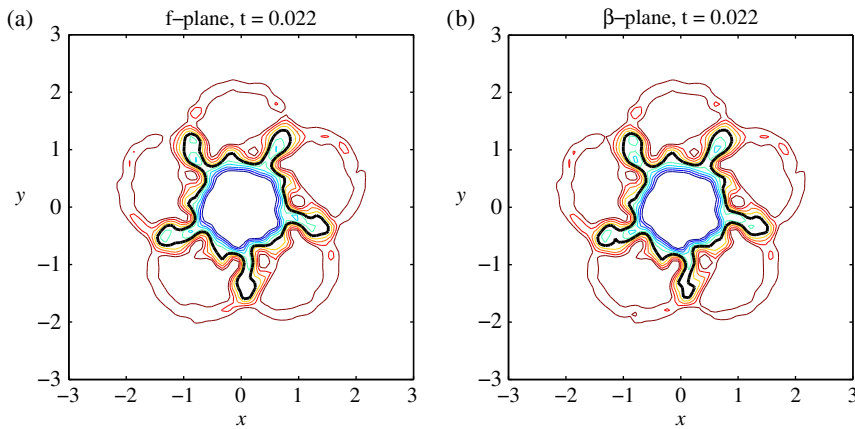


FIGURE 7. Pressure contour plots with interfacial pressure in bold for a mode 5 perturbation with perturbation amplitude $a = 0.5$ at time $t = 0.022$ for (a) f -plane with constant Rossby number $Ro_T = 0.1$ and (b) β -plane with Rossby number $Ro_T = 0.1$ on $y = 0$.

quadrant, the contour $p = 0.98$ in the south-west quadrant and the interfacial contour directed to the south and west.

This similarity can be explained by comparing the magnitudes of the change in Rossby number over the entire plane region. When $Ro_T = 0.1$ at $y = 0$, $Ro_T = 0.0667$ and $Ro_T = 0.2001$ at $y = 3$ and $y = -3$, respectively and, therefore, the magnitude of the change in Rossby number over the region $-3 < y < 3$ is 0.1334 compared to 1.7051 for $Ro_T = 0.15$. This smaller range in Rossby numbers for the β -plane approximation with $Ro_T = 0.1$ at $y = 0$ demonstrates that the velocity at any given point on the β -plane is of the same order as that on the f -plane for that given location. Therefore, significant differences between the two approximations would not be anticipated in mid-latitude regions.

The continual anticlockwise rotation of the pressure system causes the finger structures to detach from the main system, resulting in pockets of low pressure ranging from $p = 0.94$ to $p = 0.97$. As expected, the number of these pressure regions correspond to the perturbation mode n . What was unexpected is that beyond the time at which the finger structures detached to form these lows a new secondary finger structure started to form. This behaviour was observed for all perturbation modes and amplitudes looked at in this study. However, this phenomenon is best illustrated using a mode nine perturbation and amplitude $a = 0.5$. For this configuration, fully formed finger structures occurred at $t = 0.012$ and fully developed secondary fingers were observed at time $t = 0.019$. The secondary finger growth is smaller in amplitude and emerges from the troughs between the initial finger growth. The initial and secondary finger formation is shown in Figures 8(a) and 8(c), respectively. Figure 8(b) shows the pressure contours at the intermediate time $t = 0.014$, between the formation of the two different finger structures, and clearly shows the initial finger detachment.

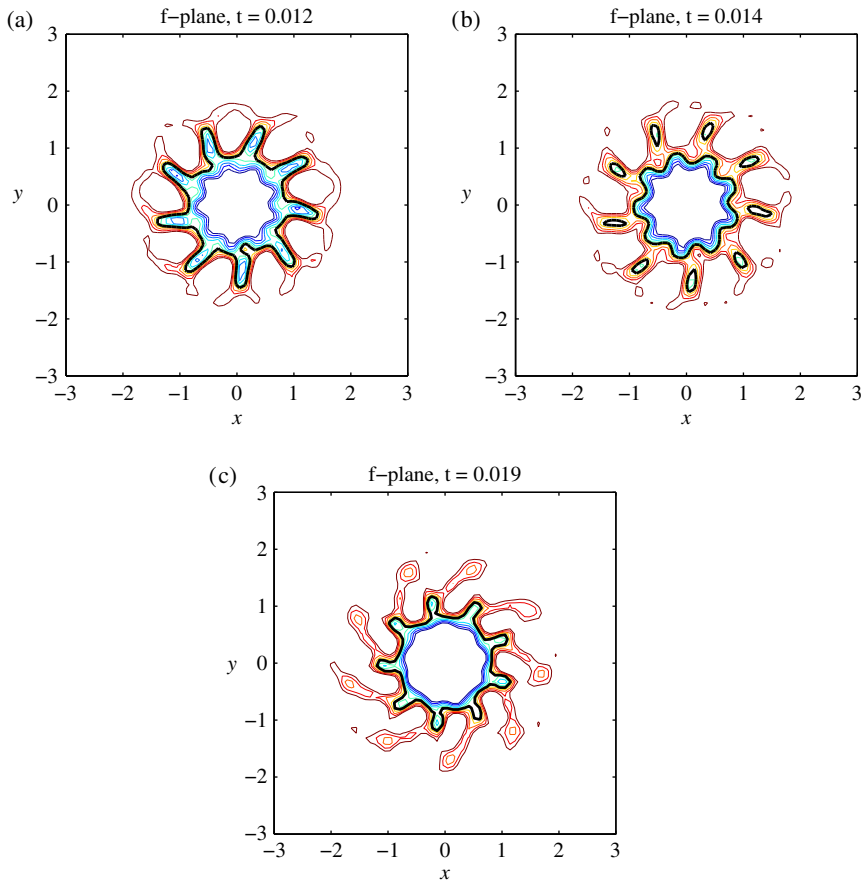


FIGURE 8. Pressure contour plots with interfacial contour in bold for a mode 9 perturbation with perturbation amplitude $a = 0.5$ and Rossby number $Ro_T = 0.15$ on the f -plane at times (a) $t = 0.012$, (b) $t = 0.014$ and (c) $t = 0.019$.

Similar results are obtained for all perturbation modes considered in this paper with $Ro_T = 0.15$, although the times at which fully formed finger structures occur differ slightly. When the perturbation amplitude is the same, the time for finger formation is marginally increased as the perturbation mode decreases. An example of this is shown in Figure 9. Finger structures have completely formed at time $t = 0.015$ for a mode seven perturbation (Figure 9(a)), compared to $t = 0.019$ for the decreased mode five perturbation (Figure 9(b)). If the Rossby number is decreased to $Ro_T = 0.1$ and the perturbation mode and amplitude are the same, it was found that the time to develop finger structures increased, although the structure is not as well defined.

Changing the initial perturbation amplitude a , also has impacts on the formation of finger structures. If the initial amplitude of the perturbation was decreased to $a = 0.25$, then the time for finger formation also decreased. To illustrate this point, Figure 10

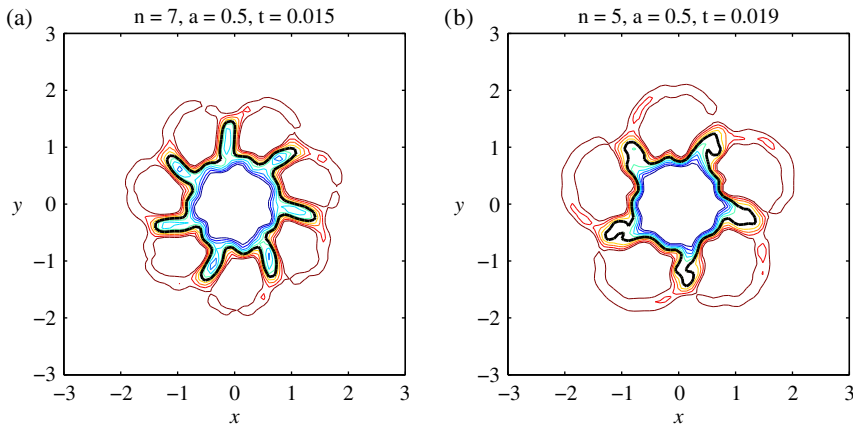


FIGURE 9. Pressure contour plots with interfacial contour in bold, perturbation amplitude $a = 0.5$ and $Ro_T = 0.15$ on the f -plane for (a) mode 7 perturbation at time $t = 0.015$ and (b) mode 5 perturbation at time $t = 0.019$.

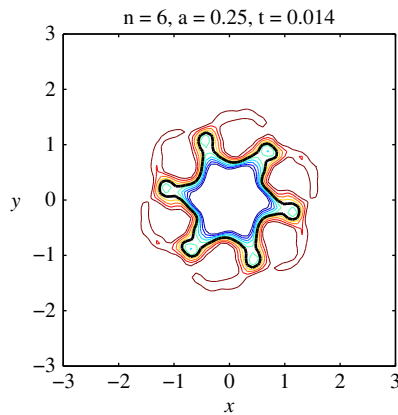


FIGURE 10. Pressure contour plot with interfacial pressure in bold, perturbation amplitude $a = 0.25$ and $Ro_T = 0.15$ on the f -plane for a mode 6 perturbation at time $t = 0.014$.

shows the fully formed fingers for a mode six perturbation with reduced amplitude $a = 0.25$ at time $t = 0.014$, whereas for a mode six perturbation with amplitude $a = 0.5$ the fingers formed at $t = 0.018$, as presented in Figure 6(a). When the perturbation amplitude decreases further to $a = 0.1$, the previously observed finger structures do not eventuate in this case.

The contour plots presented above have used $M = N = 31$ Fourier coefficients and 101 grid points in each spatial variable. To justify using these values we have investigated different grid resolutions and truncations in the Fourier series representations. Increasing the grid size to 151×151 has no influence on the numerical

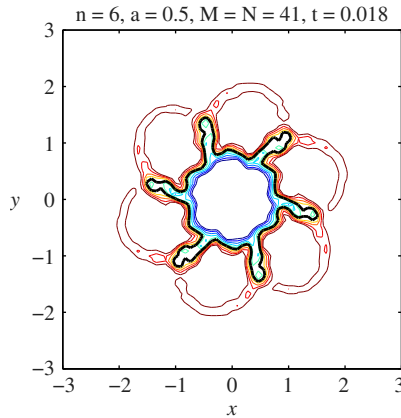


FIGURE 11. Pressure contour plot with interfacial pressure in bold for a mode 6 perturbation and perturbation amplitude $a = 0.5$ at time $t = 0.018$ on the f -plane with constant Rossby number $Ro_T = 0.15$ and $M = N = 41$ Fourier coefficients.

solution. Figure 11 shows the contour map for the same parameters as in Figure 6(a) except that $M = N = 41$ Fourier coefficients were used in the numerical calculations. Comparing these two figures directly, we can conclude that introducing higher Fourier modes suggests that our numerical solution when $M = N = 31$ has converged, as there are only small-scale changes in the tips of the finger structures.

Furthermore, an analysis of the Fourier coefficients with increasing mode number n has been undertaken, by fitting a straight line on a log–log plot (logarithmic diagram). This reveals that the coefficients decay approximately as n^{-2} . An example log–log plot for $|P_{mn}(t)|$ is shown in Figure 12, for the case $m = 1$ at time $t = 0.020$. In this instance, every second coefficient is zero and so has been omitted; the first few coefficients are also not shown, since it is only the later ones that are of interest. The coefficients are drawn with (blue, colour online) asterisks, and the (red) dashed line is the “best fit” line, with slope -2.16 .

All the simulations so far have consisted of a single mode perturbation. However, considering an initial pressure and density of the form

$$p(x, y, 0) = \rho(x, y, 0) = \begin{cases} 1 & \text{if } r > 1 + f(\theta) \\ 1 - \mu & \text{if } r < 1 + f(\theta), \end{cases} \tag{4.4}$$

where

$$f(\theta) = \frac{2a}{\pi} [\arcsin(\sin(m\theta))]$$

produces a triangle wave perturbation. With $m = 2$ and perturbation amplitude $a = 0.5$, the Fourier series representation of $f(\theta)$ is multimodal and takes the form

$$f(\theta) = \frac{16}{\pi^2} \sum_{k=1}^{\infty} \frac{(-1)^{k+1} \sin[(4k - 2)\theta]}{(4k - 2)^2}.$$

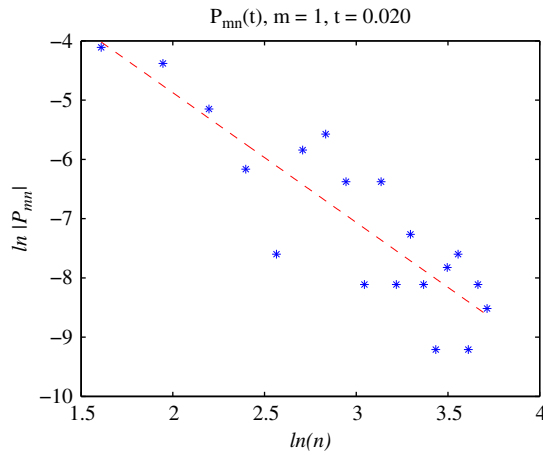


FIGURE 12. Log–log plot of the pressure variable Fourier coefficients $P_{mn}(t)$ with $M = N = 41$ at time $t = 0.020$ for $m = 1$. Dashed red line is the line of best fit with slope equal to negative 2.16 (colour available online).

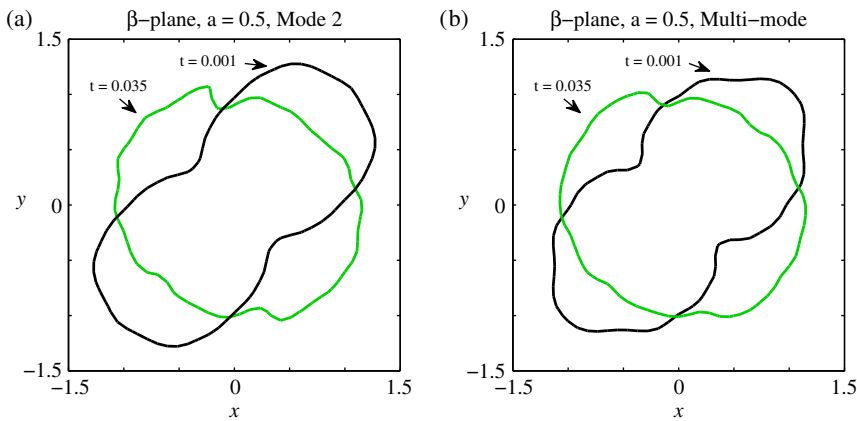


FIGURE 13. Interfacial pressure plot on the β -plane with perturbation amplitude $a = 0.5$ and Rossby number $Ro_T = 0.15$ at times $t = 0.001$ and 0.035 for a (a) Mode 2 perturbation and (b) Multi-mode perturbation with $m = 2$.

The results from applying a multimodal perturbation (4.4) are similar to those achieved using a sinusoidal perturbation (4.2). Figure 13(a) shows the interfacial pressure on the β -plane for a mode two perturbation at times $t = 0.001$ and $t = 0.035$ and there is close resemblance to a multimodal perturbation when $m = 2$ at the same times shown in Figure 13(b). The higher modes seem to smooth out the interfacial contours as time increases.

5. Conclusions and discussion

In this paper, we have focused on the structure of large-scale vortices in the atmosphere that initially have a perturbed sinusoidal structure. As time passes, these perturbations grow to form wave-like fingers. The aim was firstly to look at what conditions are most favourable for these perturbations to grow and form large-scale finger formations on the outer edges of the pressure system. Secondly, the role of the f -plane and β -plane approximations on finger development has been studied. In the f -plane approximation, the Coriolis acceleration is assumed to be constant; whereas it varies with latitude in the β -plane theory. The greatest difference between both approximations is seen at the extremities of the planes. This is to be expected as the β -effect is more noticeable further away from the f -plane tangent latitude.

The observation data that initially inspired the work in this paper shows the fingers spiralling out and travelling in the same direction as the system's rotation, owing to the fluid velocity being greater on the outer edges of the pressure system (see Figure 1). However, as shown in this paper, the fingers spiral out in the opposite direction as the fluid velocity is larger in the centre of the pressure system.

By considering Rossby numbers $Ro_T = 0.1$ and $Ro_T = 0.15$, we have focused on the accuracy of the approximate models in the mid-latitude and mid-low latitude regions. If $Ro_T = 0.1$, then the origin of the approximation for both the f -plane and β -plane is located along the latitude $\phi \approx 43.3^\circ$ corresponding to a mid-latitude region. If $Ro_T = 0.15$ we are looking at regions centred at about the mid-low latitude $\phi \approx 27.2^\circ$. In the mid-latitude regions the results for both the f -plane and β -plane are almost identical. At lower latitudes the β -effect is more pronounced due to the greater range of Rossby numbers. Therefore, we conclude that in mid-latitude regions the f -plane approximation is sufficiently accurate to be able to ignore the β -effect, whereas in the mid-low latitude regions the β -effect is more pronounced.

We have also taken the time to initial finger formation to be the latest time at which the interfacial pressure contour $p = 0.95$ has one closed contour. Beyond this time, the finger tips detach to form pockets of low pressure that dissipate in time as secondary finger structures form. The time at which secondary finger structures occur is taken to be when there is again one closed interfacial pressure contour.

The initial condition for pressure has a substantial impact on the subsequent development of the finger formations on the outer regions of the pressure system. Several different perturbation modes have been investigated throughout this paper. The higher the perturbation mode, the more pronounced is the finger structure formed. This was especially the case for the largest perturbation amplitude of $a = 0.5$. For the lowest perturbation amplitude $a = 0.1$ the finger structure was nonexistent.

The original motivation for this paper as seen in Figure 1 was a low-pressure system in the southern hemisphere. However, we have presented results for low-pressure systems in the northern hemisphere. We have also generated these results for southern hemisphere systems ($f < 0$), although these are not shown here. They are found to be identical, except for the fact that they are reflected about the centre line $y = 0$.

Acknowledgements

The work of the first author is supported by a Tasmania Graduate Research Scholarship. The authors are grateful to the Australian Bureau of Meteorology for being able to use their satellite images, and in particular to Mike Willmott for retrieving the data. Assistance from Anita Griffin with proof reading and editing is gratefully acknowledged.

References

- [1] G. R. Baker and L. D. Pham, “A comparison of blob methods for vortex sheet roll-up”, *J. Fluid Mech.* **547** (2006) 297–316; doi:10.1017/S0022112005007305.
- [2] R. E. Caffisch, X. Li and M. J. Shelley, “The collapse of an axi-symmetric, swirling vortex sheet”, *Nonlinearity* **6** (1993) 843–867; doi:10.1088/0951-7715/6/6/001.
- [3] S. Chandrasekhar, *Hydrodynamic and hydromagnetic stability* (Dover, New York, 1981).
- [4] M. J. Chen and L. K. Forbes, “Accurate methods for computing inviscid and viscous Kelvin–Helmholtz instability”, *J. Comput. Phys.* **230** (2011) 1499–1515; doi:10.1016/j.jcp.2010.11.017.
- [5] S. J. Cowley, G. R. Baker and S. Tanveer, “On the formation of Moore curvature singularities in vortex sheets”, *J. Fluid Mech.* **378** (1999) 233–267; doi:10.1017/S0022112098003334.
- [6] G. D. Crapper, N. Dombrowski and G. A. D. Pyott, “Kelvin–Helmholtz wave growth on cylindrical sheets”, *J. Fluid Mech.* **68** (1975) 497–502; doi:10.1017/S0022112075001784.
- [7] P. G. Drazin and W. H. Reid, *Hydrodynamic stability*, 2nd edn. (Cambridge University Press, Cambridge, 2004).
- [8] L. K. Forbes, “The Rayleigh–Taylor instability for inviscid and viscous fluids”, *J. Engrg. Math.* **65** (2009) 273–290; doi:10.1007/s10665-009-9288-9.
- [9] L. K. Forbes, “A cylindrical Rayleigh–Taylor instability: radial outflow from pipes or stars”, *J. Engrg. Math.* **70** (2011) 205–224; doi:10.1007/s10665-010-9374-z.
- [10] L. K. Forbes and J. M. Cosgrove, “A line vortex in a two-fluid system”, *J. Engrg. Math.* **84** (2014) 181–199; doi:10.1007/s10665-012-9606-5.
- [11] J. R. Holton, *An introduction to dynamic meteorology*, 3rd edn. (Academic Press, Cambridge, 1992).
- [12] J. M. Kay and R. M. Nedderman, *Fluid mechanics and transfer processes* (Cambridge University Press, Cambridge, 1985).
- [13] R. Krasny, “Desingularization of periodic vortex sheet roll-up”, *J. Comput. Phys.* **65** (1986) 292–313; doi:10.1016/0021-9991(86)90210-X.
- [14] F. B. Lipps, “A note on the beta-plane approximation”, *Tellus* **16** (1964) 535–537; doi:10.1111/j.2153-3490.1964.tb00190.x.
- [15] C. Matsuoka and K. Nishihara, “Analytical and numerical study on a vortex sheet in incompressible Richtmyer–Meshkov instability in cylindrical geometry”, *Phys. Rev. E* **74** (2006) 066303–066314; doi:10.1103/PhysRevE.74.066303.
- [16] D. W. Moore, “The spontaneous appearance of a singularity in the shape of an evolving vortex sheet”, *Proc. R. Soc. Lond. A* **365** (1979) 105–119 doi:10.1098/rspa.1979.0009.
- [17] G. K. Vallis, *Atmospheric and oceanic fluid dynamics* (Cambridge University Press, Cambridge, 2006).
- [18] G. von Winckel, lgwt.m, at: MATLAB file exchange website, <http://www.mathworks.com/matlabcentral/fileexchange/4540-legendre-gauss-quadrature-weights-and-nodes>, 2004.